MATHEMATICAL BIOSCIENCES
AND ENGINEERING
Volume **8**, Number **3**, July **2011**

doi:10.3934/mbe.2011.8.785

pp. **785–806**

NUMERICAL CHARACTERIZATION OF HEMODYNAMICS CONDITIONS NEAR AORTIC VALVE AFTER IMPLANTATION OF LEFT VENTRICULAR ASSIST DEVICE

Annalisa Quaini

Department of Mathematics, University of Houston
4800 Calhoun Rd, Houston (TX) 77204, USA

Sunčica Čanić

Department of Mathematics, University of Houston
4800 Calhoun Rd, Houston (TX) 77204, USA

David Paniagua

Department of Cardiology, Texas Heart Institute at St. Lukes Episcopal Hospital
and Mickael E Debakey VA Medical Center
2002 Holcombe Boulevard, Houston, TX 77030

(Communicated by Mette Olufsen)

Abstract. Left Ventricular Assist Devices (LVADs) are implantable mechanical pumps that temporarily aid the function of the left ventricle. The use of LVADs has been associated with thrombus formation next to the aortic valve and close to the anastomosis region, especially in patients in which the native cardiac function is negligible and the aortic valve remains closed. Stagnation points and recirculation zones have been implicated as the main fluid dynamics factors contributing to thrombus formation. The purpose of the present study was to develop and use computer simulations based on a fluid-structure interaction (FSI) solver to study flow conditions corresponding to different strategies in LVAD ascending aortic anastomosis providing a scenario with the lowest likelihood of thrombus formation. A novel FSI algorithm was developed to deal with the presence of multiple structures corresponding to different elastic properties of the native aorta and of the LVAD cannula. A sensitivity analysis of different variables was performed to assess their impact of flow conditions potentially leading to thrombus formation. It was found that the location of the anastomosis closest to the aortic valve (within 4 cm away from the valve) and at the angle of 30° minimizes the likelihood of thrombus formation. Furthermore, it was shown that the rigidity of the dacron anastomosis cannula plays almost no role in generating pathological conditions downstream from the anastomosis. Additionally, the flow analysis presented in this manuscript indicates that compliance of the cardiovascular tissue acts as a natural inhibitor of pathological flow conditions conducive to thrombus formation and should not be neglected in computer simulations.

2000 *Mathematics Subject Classification.* Primary: 65M60, 74F10, 76D05.

Key words and phrases. Fluid-structure interaction, structure-structure interaction, monolithic methods, semi-implicit coupling, hemodynamics.

The authors acknowledge the support received by grants NSF DMS-0806941, Texas Education Board ARP - Mathematics 003652-0051-2006, and NSF/NIH (NIGMS) DMS-0443826.

1. **Introduction.** Left Ventricular Assist Devices (LVADs) are implantable mechanical pumps that temporarily aid the function of the left ventricle as a bridge to recovery or transplant. In some patients they are used as destination therapy. The use of LVADs has been associated with thrombus formation next to the aortic valve and close to the anastomosis region, especially in patients in which the native cardiac function is negligible and the aortic valve remains closed [9, 10, 14, 16, 20, 23]. Stagnation points and recirculation zones have been implicated as the main fluid dynamics factors contributing to thrombus formation [7, 12, 13, 22]. The purpose of our study was to develop and use computer simulations based on a fluid-structure interaction solver to investigate formation of stagnation points and recirculation zones near the anastomosis region and the aortic valve for several locations and angles of the anastomisis cannula. In contrast with other works which include only a study of the region near the anastomosis, ignore the aortic valve location, and almost exclusively ignore the compliance of the arterial wall, the present study shows that all these factors are important in the optimal LVAD cannula placement analysis.

A fluid-structure interaction (FSI) solver, originally developed by Badia, Quaini and Quarteroni in [2, 4], was extended in the present work to include structures with different elastic wall properties modeling different compliant behaviors of the ascending aorta and of the anastomosis cannula. In this manuscript a semi-implicit monolithic approach is proposed to handle all the interactions at the same time. At all the interfaces (fluid-structure and structure-structure) the coupling conditions are treated in the same way: weak treatment of the continuity of stresses and strong treatment of the continuity of velocity. The monolithic fluid-structure interaction system, obtained after space-time discretization and linearization in a fixed point approach, is preconditioned with a diagonal scaling and an ILUT preconditioner [2]. The system is then solved by a Krylov method. This approach is stable and convergent even in the case when the structure and the fluid have comparable densities, which is the case in the blood flow applications.

The analysis of flow conditions between the anastomosis and the aortic leaflets suggests that the optimal placement of the anastomosis cannula is the one which is closest to the aortic valve (lower that the usual placement of 5 cm away from the valve region) and sutured at the angle of 30° to the ascending aorta. This strategy provides the lowest likelihood of stagnant flow formation near the (closed) aortic valve, and the smallest deviation from laminar flow downstream from the anastomosis. Furthermore, it was shown that the rigidity of the dacron anastomosis cannula plays almost no role in generating pathological conditions downstream from the anastomosis. Additionally, the flow analysis presented in this manuscript indicates that compliance of the cardiovascular tissue acts as a natural inhibitor of pathological flow conditions conducive to thrombus formation and should not be neglected in the computer simulations.

Details are presented in the following sections. The numerical method is described in Section 2. Section 3 discusses the LVAD ascending aortic anastomosis problem. Sections 4 and 5 discuss numerical findings regarding the influence of the placement of LVAD cannula on the blood flow conditions quantified by the introduction of the vorticity index and the stagnation index. Section 6 contains the conclusions.

2. **The Numerical method.** In this work a semi-implicit monolithic method is proposed for the solution of fluid-structure interaction problems in the presence of structures with different material properties. The basic features of the proposed approach concern the mathematical formulation of fluid and structure problems in terms of velocities, the use of a single finite element partition for the whole domain and the use of the same finite element space for fluid and structure subproblems. At both fluid-structure and structure-structure interfaces the subproblems are coupled by two transmission conditions: continuity of velocity (kinematic condition) and continuity of stress (dynamic condition). At all the interfaces those conditions are imposed in the same way: the dynamic coupling condition is satisfied in the weak sense, and the kinematic one in the strong sense.

Nonlinearities in the resulting coupled problem are dealt via a fixed point approach in an explicit way. This means that only one iteration of the linearization technique is performed at every time step. It was shown in [17] that nonlinear iterations can be disregarded without endangering stability thereby allowing important computational time savings. A FSI algorithm in which the fluid-structure coupling is treated implicitly and the nonlinearities are treated explicitly is said to be semi-implicit.

The solution of the resulting linearized monolithic system is preconditioned in two steps. First a diagonal scaling of the FSI matrix is performed, and then the GMRES method is used to solve the resulting system which is preconditioned by an incomplete LU factorization of the diagonally scaled matrix (the ILUT preconditioner). It was shown in [2] that the ILUT-GMRES method performs well even in the case when the density of the fluid is close to that of the structure, which is the case in the blood flow applications.

A detailed description of the method is presented next.

2.1. **Problem definition.** Denote by $\Omega_t \subset \mathbb{R}^d$, d=2,3, and $t \in [0,T]$, a bounded, time-dependent domain consisting of a subdomain Ω_t^f occupied by a fluid, and N_s subdomains Ω_t^i, $i = 1, ..., N_s$, determined by solid structures, so that $\Omega_t = \Omega_t^f \cup \Omega_t^1 ... \cup \Omega_t^{N_s}$. We suppose that each structure subdomain shares a part of the boundary with the fluid domain boundary $\partial\Omega_t^f$. These common boundaries are the fluid-structure interfaces Σ_t^{fi}, i.e. $\Sigma_t^{fi} = \partial\Omega_t^f \cap \partial\Omega_t^i$, $i = 1, ..., N_s$. For two neighboring structures Ω_t^i and Ω_t^j, the solid-solid interface is denoted by $\Sigma_t^{ij} = \partial\Omega_t^i \cap \partial\Omega_t^j$ (see Figure 1). The initial configuration Ω_0 at $t = 0$ is considered as the reference one. We are interested in the flow of an incompressible, viscous, Newtonian fluid in a domain bounded by linearly elastic structures.

The fluid problem is governed by the incompressible Navier-Stokes equations

$$\partial_t \boldsymbol{u} + \boldsymbol{u} \cdot \nabla \boldsymbol{u} - \frac{1}{\rho_f} \nabla \cdot \boldsymbol{\sigma}_f = \boldsymbol{f}_f \qquad \text{in } \Omega_t^f \times (0,T),$$

$$\nabla \cdot \boldsymbol{u} = 0 \qquad \text{in } \Omega_t^f \times (0,T),$$

where $\boldsymbol{u}$ is the fluid velocity, $\boldsymbol{\sigma}_f$ the Cauchy stress tensor and $\boldsymbol{f}_f$ the body force. For Newtonian fluids $\boldsymbol{\sigma}_f$ has the following expression

$$\boldsymbol{\sigma}_f(\boldsymbol{u}, p) = -p\mathbf{I} + 2\mu\boldsymbol{\epsilon}(\boldsymbol{u}),$$

where p is the pressure, μ is the fluid viscosity, and

$$\boldsymbol{\epsilon}(\boldsymbol{u}) = \frac{1}{2}(\nabla \boldsymbol{u} + (\nabla \boldsymbol{u})^T)$$

is the strain rate tensor, with ∇ denoting the spatial gradient operator.

The mechanical behavior of the i-th structure is governed by the elastodynamics equation

$$D_t^2 \boldsymbol{\eta}_i - \frac{1}{\rho_i} \nabla \cdot \boldsymbol{\sigma}_i = \boldsymbol{f}_i \qquad \text{in } \Omega_t^i \times (0,T), \tag{1}$$

where $\boldsymbol{\eta}_i$ is the structure displacement, $\boldsymbol{f}_i$ the body force, and D_t denotes the material derivative. Equation (1) must be supplemented with a constitutive law that relates Cauchy stress tensor $\boldsymbol{\sigma}_i$ with strain $\boldsymbol{\epsilon}(\boldsymbol{\eta}_i)$. As a simple example, in our numerical simulations we adopt the linear Saint-Venant Kirchhoff elastic model (isotropic, hyperelastic material), for which the consitutive law reads as follows:

$$\boldsymbol{\sigma}_i(\boldsymbol{\epsilon}(\boldsymbol{\eta}_i)) = 2\mu_\ell^i \boldsymbol{\epsilon}(\boldsymbol{\eta}_i) + \lambda_\ell^i \mathrm{tr}(\boldsymbol{\epsilon}(\boldsymbol{\eta}_i))\mathbf{I},$$

where μ_ℓ^i and λ_ℓ^i are the Lamé constants of the i-th structure. We employ the linear strain-displacement relationship given by $\boldsymbol{\epsilon}(\boldsymbol{\eta}_i) = (\nabla \boldsymbol{\eta}_i + (\nabla \boldsymbol{\eta}_i)^T)/2$ which then leads to the Cauchy stress-displacement relationship of the following form

$$\boldsymbol{\sigma}_i(\boldsymbol{\eta}) = \mu_\ell^i (\nabla \boldsymbol{\eta}_i + (\nabla \boldsymbol{\eta}_i)^T) + \lambda_\ell^i (\nabla \cdot \boldsymbol{\eta}_i)\mathbf{I}.$$

It will be assumed in this manuscript that the mechanical properties of the structures differ only by the values of the coefficients ρ_i, μ_ℓ^i, and λ_ℓ^i. Of course, other structure models can be chosen according to the specific problem under consideration.

At Σ_t^{fi}, the fluid and structure subproblems are coupled via the kinematic and dynamic coupling conditions: the continuity of velocity (kinematic coupling condition)

$$\boldsymbol{u} = \partial_t \boldsymbol{\eta}_i \quad \text{on } \Sigma_t^{fi} \times (0,T),\ i = 1, ..., N_s$$

and balance of stresses (dynamic coupling condition):

$$\boldsymbol{\sigma}_i \cdot \boldsymbol{n}_i + \boldsymbol{\sigma}_f \cdot \boldsymbol{n}_f = 0 \quad \text{on } \Sigma_t^{fi} \times (0,T),\ i = 1, ..., N_s.$$

Here, $\boldsymbol{n}_f$ denotes the outward normal to Ω_t^f, and $\boldsymbol{n}_i$ denotes the outward normal to the i-th structure domain boundary. The same contact conditions hold at the interface between two structures:

$$\begin{aligned} \partial_t \boldsymbol{\eta}_i &= \partial_t \boldsymbol{\eta}_j && \text{on } \Sigma_t^{ij} \times (0,T), \\ \boldsymbol{\sigma}_i \cdot \boldsymbol{n}_i + \boldsymbol{\sigma}_j \cdot \boldsymbol{n}_j &= 0 && \text{on } \Sigma_t^{ij} \times (0,T). \end{aligned}$$

To capture the time-evolution of the whole domain Ω_t an Arbitrary Lagrangian-Eulerian (ALE) approach is considered. More precisely, define the following two families of mappings:

$$\begin{aligned} \mathcal{L}^i \ : \ \Omega_0^i \times [0,T] &\longrightarrow \Omega_t^i, \\ (\boldsymbol{x}_0, t) &\longrightarrow \boldsymbol{x} = \mathcal{L}^i(\boldsymbol{x}_0, t), \end{aligned} \tag{2}$$

and

$$\begin{aligned} \mathcal{A} \ : \ \Omega_0^f \times [0,T] &\longrightarrow \Omega_t^f, \\ (\boldsymbol{x}_0, t) &\longrightarrow \boldsymbol{x} = \mathcal{A}(\boldsymbol{x}_0, t). \end{aligned} \tag{3}$$

The map $\mathcal{L}_t^i = \mathcal{L}_i(\cdot, t)$ tracks the i-th structure domain in time while $\mathcal{A}_t = \mathcal{A}(\cdot, t)$ tracks the fluid domain. The two must agree on the interfaces:

$$\begin{aligned} &\mathcal{L}_t^i = \mathcal{A}_t \quad \text{on } \Sigma_t^{fi},\ i = 1, ..., N_s, \\ &\mathcal{L}_t^i = \mathcal{L}_t^j \quad \text{on } \Sigma_t^{ij},\ \text{if } \partial\Omega_t^i \cap \partial\Omega_t^j \neq \emptyset,\ i, j = 1, ..., N_s. \end{aligned} \tag{4}$$

See Figure 1. The mapping $\mathcal{L}_t^i$ is defined (in Lagrangian framework) as:

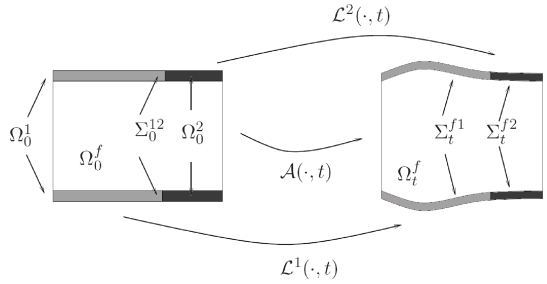

FIGURE 1. Parametrization of the domain.

$$\mathcal{L}_t^i(\boldsymbol{x}_0) = \boldsymbol{x}_0 + \hat{\boldsymbol{\eta}}_i(\boldsymbol{x}_0, t),$$

where the "hat" denotes a variable evaluated at the reference configuration. The mapping $\mathcal{A}_t$ can be defined as an appropriate extension operator to Ω_t^f of its values on the interfaces:

$$\mathcal{A}_t(\boldsymbol{x}_0) = \boldsymbol{x}_0 + \text{Ext}(\hat{\boldsymbol{\eta}}_i(\boldsymbol{x}_0, t)|_{\Sigma_0^{fi}}), \quad i = 1, ..., N_s.$$

A classical choice for the extension operator is to consider a harmonic extension in the reference domain. $\mathcal{A}_t$ is called the Arbitrary Lagrangian-Eulerian (ALE) mapping [11]. The ALE derivative of the fluid velocity is then defined as:

$$\partial_t \boldsymbol{u}|_{\boldsymbol{x}_0} = \partial_t \boldsymbol{u} + \boldsymbol{w} \cdot \nabla \boldsymbol{u},$$

where the domain velocity $\boldsymbol{w}$ is calculated using the following expression:

$$\boldsymbol{w}(\boldsymbol{x}, t) = \partial_t \boldsymbol{x}|_{\boldsymbol{x}_0} = \partial_t \mathcal{A}_t \circ \mathcal{A}_t^{-1}(\boldsymbol{x}).$$

The **fluid-structure interaction problem with multiple structures in strong form** is defined as follows:

(i) Geometry: find the fluid domain displacement so that

$$\begin{aligned} &\mathcal{A}_t(\boldsymbol{x}_0) = \boldsymbol{x}_0 + \text{Ext}(\hat{\boldsymbol{\eta}}_i|_{\Sigma_0^{fi}}), i = 1, ..., N_s, \\ &\boldsymbol{w} = \partial_t \mathcal{A}_t \circ \mathcal{A}_t^{-1}, \quad \Omega_t^f = \mathcal{A}_t(\Omega_0^f). \end{aligned} \tag{5}$$

(ii) Fluid-structure itneraction: find velocity $\boldsymbol{u}$, pressure p and displacement $\boldsymbol{\eta}_i$, $i = 1, ..., N_s$, such that

$$\partial_t \boldsymbol{u}|_{\boldsymbol{x}_0} + (\boldsymbol{u} - \boldsymbol{w}) \cdot \nabla \boldsymbol{u} - \frac{1}{\rho_f} \nabla \cdot \boldsymbol{\sigma}_f = \boldsymbol{f}_f \quad \text{in } \Omega_t^f \times (0,T), \tag{6a}$$

$$\nabla \cdot \boldsymbol{u} = 0 \quad \text{in } \Omega_t^f \times (0,T), \tag{6b}$$

$$D_t^2 \boldsymbol{\eta}_i - \frac{1}{\rho_i} \nabla \cdot \boldsymbol{\sigma}_i = \boldsymbol{f}_i, \quad \text{in } \Omega_t^i \times (0,T), \ = 1, ..., N_s, \tag{6c}$$

$$\boldsymbol{u} = \partial_t \boldsymbol{\eta}_i, \quad \text{on } \Sigma_t^{fi} \times (0,T), \ i = 1, ..., N_s, \tag{6d}$$

$$\boldsymbol{\sigma}_i \cdot \boldsymbol{n}_i + \boldsymbol{\sigma}_f \cdot \boldsymbol{n}_f = 0, \quad \text{on } \Sigma_t^{fi} \times (0,T), \ i = 1, ..., N_s, \tag{6e}$$

$$\partial_t \boldsymbol{\eta}_i = \partial_t \boldsymbol{\eta}_j, \quad \text{on } \Sigma_t^{ij} \times (0,T), \text{ if } \partial\Omega_t^i \cap \partial\Omega_t^j \neq \emptyset, \ i,j = 1, ..., N_s, \tag{6f}$$

$$\boldsymbol{\sigma}_i \cdot \boldsymbol{n}_i + \boldsymbol{\sigma}_j \cdot \boldsymbol{n}_j = 0, \quad \text{on } \Sigma_t^{ij} \times (0,T), \text{ if } \partial\Omega_t^i \cap \partial\Omega_t^j \neq \emptyset, \ i,j = 1, ..., N_s. \tag{6g}$$

Problem (6) needs to be supplemented by initial and boundary condition. Since the particular form of the initial and boundary conditions does not influence the rest of the discussion in this section, it will be omitted. The initial and boundary conditions for the specific problem discussed in this manuscript will be specified in Section 3.

2.2. **Weak formulation.** In order to define the variational formulation of the fluid-structure interaction problem (5)-(6), denote with $L^2(\Omega)$ the space of square integrable functions in Ω and with $H^1(\Omega)$ the space of functions in $L^2(\Omega)$ with first derivatives in $L^2(\Omega)$. Furthermore, denote by $(\cdot,\cdot)_\Omega$ and $\langle \cdot,\cdot \rangle_\Omega$ the L^2-product and a duality pairing in L^2, respectively.

For simplicity, let the number of different structures equal to 2, $N_s = 2$ (see Figure 1). The following spaces will be used bellow:

$$\begin{aligned}
V^f(t) &= \left\{ \boldsymbol{v} : \Omega_t^f \to \mathbb{R}^d, \ \boldsymbol{v} = \hat{\boldsymbol{v}} \circ (\mathcal{A}_t)^{-1}, \hat{\boldsymbol{v}} \in (H^1(\Omega_0^f))^d \right\}, \\
V_0^f(t) &= \left\{ \boldsymbol{v} \in V^f(t), \ \boldsymbol{v}|_{\Sigma_t^{fi}} = \boldsymbol{0}, \ i = 1, ..., N_s \right\}, \\
Q(t) &= \left\{ q : \Omega_t^f \to \mathbb{R}, \ q = \hat{q} \circ (\mathcal{A}_t)^{-1}, \ \hat{q} \in L^2(\Omega_0^f) \right\}, \\
\hat{V}^i &= \left\{ \hat{\boldsymbol{v}} : \Omega_0^i \to \mathbb{R}^d, \ \hat{\boldsymbol{v}} \in (H^1(\Omega_0^i))^d \right\}, \ i = 1, 2, \\
\hat{V}_0^2 &= \left\{ \boldsymbol{v} \in \hat{V}^2, \ \boldsymbol{v}|_{\Sigma_0^{12}} = \boldsymbol{0} \right\}.
\end{aligned}$$

$\mathcal{A}_t^{-1}$ is assumed Lipschitz continuous in order for $V^f(t) \subset (H^1(\Omega_t^f))^d$ and $Q(t) \subset L^2(\Omega_t^f)$. We introduce the following notation:

$$\begin{aligned}
\mathcal{N}(\boldsymbol{a}; \boldsymbol{u}, p, \boldsymbol{v}, q)_\Omega =& 2\mu \left(\boldsymbol{\epsilon}(\boldsymbol{u}), \boldsymbol{\epsilon}(\boldsymbol{v}) \right)_\Omega + \rho_f \int_\Omega (\boldsymbol{a} \cdot \nabla \boldsymbol{u}) \cdot \boldsymbol{v} \, \mathrm{d}\Omega - (p, \nabla \cdot \boldsymbol{v})_\Omega \\
&+ (\nabla \cdot \boldsymbol{u}, q)_\Omega .
\end{aligned}$$

The **weak formulation of the fluid-multi structure interaction problem** is then given by: find $(\boldsymbol{u}, p, \hat{\boldsymbol{\eta}}_1, \hat{\boldsymbol{\eta}}_2) \in V^f(t) \times Q(t) \times \hat{V}^1 \times \hat{V}^2$ for a given $t \in (0,T)$

such that

$$\rho_f \left(\partial_t \boldsymbol{u}|_{\boldsymbol{x}_0}, \boldsymbol{v}_0^f \right)_{\Omega_t^f} + \mathcal{N}(\boldsymbol{u}-\boldsymbol{w}; \boldsymbol{u}, p, \boldsymbol{v}_0^f, q)_{\Omega_t^f} = \left\langle \boldsymbol{f}_f, \boldsymbol{v}_0^f \right\rangle_{\Omega_t^f}, \tag{7a}$$

$$\rho_1 \left(\partial_t^2 \hat{\boldsymbol{\eta}}_1, \hat{\boldsymbol{v}}^1 \right)_{\Omega_0^1} + \left\langle \hat{\boldsymbol{\sigma}}_1, \nabla \hat{\boldsymbol{v}}^1 \right\rangle_{\Omega_0^1} = \left\langle \hat{\boldsymbol{f}}_1, \hat{\boldsymbol{v}}^1 \right\rangle_{\Omega_0^1} - \langle \boldsymbol{\sigma}_f \cdot \boldsymbol{n}_f, \boldsymbol{v}^1 \rangle_{\Sigma_t^{f1}} - \langle \hat{\boldsymbol{\sigma}}_2 \cdot \hat{\boldsymbol{n}}_2, \hat{\boldsymbol{v}}^1 \rangle_{\Sigma_0^{12}}, \tag{7b}$$

$$\rho_2 \left(\partial_t^2 \hat{\boldsymbol{\eta}}_2, \hat{\boldsymbol{v}}_0^2 \right)_{\Omega_0^2} + \left\langle \hat{\boldsymbol{\sigma}}_2, \nabla \hat{\boldsymbol{v}}_0^2 \right\rangle_{\Omega_0^2} = \left\langle \hat{\boldsymbol{f}}_2, \hat{\boldsymbol{v}}_0^2 \right\rangle_{\Omega_0^2} - \langle \boldsymbol{\sigma}_f \cdot \boldsymbol{n}_f, \boldsymbol{v}^2 \rangle_{\Sigma_t^{f2}}, \tag{7c}$$

$$\boldsymbol{u} = \partial_t \hat{\boldsymbol{\eta}}_i \circ (\mathcal{A}_t)^{-1} \quad \text{on } \Sigma_t^{fi},\ i = 1, 2, \tag{7d}$$

$$\partial_t \hat{\boldsymbol{\eta}}_1 = \partial_t \hat{\boldsymbol{\eta}}_2 \quad \text{on } \Sigma_0^{12}, \tag{7e}$$

for all $(\boldsymbol{v}_0^f, q, \hat{\boldsymbol{v}}^1, \hat{\boldsymbol{v}}_0^2) \in V_0^f(t) \times Q(t) \times \hat{V}^1 \times \hat{V}_0^2$.

The continuity of velocities at both fluid-structure and structure-structure interfaces has been enforced in a strong way by (7d) and (7e), respectively. On the other hand, the continuity of stresses at the interfaces is imposed in a weak way via (7a)-(7c).

2.3. **The fully discrete problem: space and time discretization.** Let $\hat{V}_h^f \subset [H^1(\Omega_0^f)]^d$, $\hat{V}_{0,h}^f \subset [H_0^1(\Omega_0^f)]^d$, $\hat{Q}_h \subset L^2(\Omega_0^f)$, $\hat{V}_h^i \subset [H^1(\Omega_0^i)]^d$, and $\hat{V}_{0,h}^2 \subset [H_0^1(\Omega_0^i)]^d$ be the finite element spaces approximating V^f, V_0^f, Q, $\hat{V}^i$, and $\hat{V}_0^2$ at the reference configuration, respectively. With a slight abuse of notation denote by $V_h^f(t^n) = \mathcal{A}_{t^n}(\hat{V}_h^f)$ the finite element spaces for a given time step t^n defined via the domain mappings (2)-(3).

It is well known that the velocity-pressure finite element space (Q_h, V_h^f) is required to satisfy a discrete inf-sup condition in order to obtain pressure stability, see [6]. Thus, either inf-sup stable finite elements need to be used or a stabilization is required. In this work, a stabilized formulation, called orthogonal subgrid scales technique [8], is used to overcome both pressure instabilities and instabilities arising when the convective term is dominant. The stabilized version of the fluid problem is then obtained by replacing $\mathcal{N}$ in (7a) with

$$\mathcal{N}_s(\boldsymbol{a}_h; \boldsymbol{u}_h, p_h, \boldsymbol{v}_h, q_h)_\Omega = \mathcal{N}(\boldsymbol{a}_h; \boldsymbol{u}_h, p_h, \boldsymbol{v}_h, q_h)_\Omega + \mathcal{S}(\boldsymbol{a}_h; \boldsymbol{u}_h, p_h, \boldsymbol{v}_h, q_h)_\Omega,$$

where the perturbation term introduced by the orthogonal subgrid scales technique (in its quasi-static form) reads

$$\begin{aligned} \mathcal{S}(\boldsymbol{a}_h; \boldsymbol{u}_h, p_h, \boldsymbol{v}_h, q_h)_\Omega = &\left(\tau_1 \Pi^\perp(\boldsymbol{a}_h \cdot \nabla \boldsymbol{u}_h + \nabla p_h), \boldsymbol{a}_h \cdot \nabla \boldsymbol{v}_h + \nabla q_h\right)_\Omega \\ &+ \left(\tau_2 \Pi^\perp(\nabla \cdot \boldsymbol{u}_h), \nabla \cdot \boldsymbol{v}_h\right)_\Omega. \end{aligned} \tag{8}$$

Here, $\Pi^\perp(\cdot)$ is the L^2 orthogonal projection onto the finite element space, i. e.: $\Pi^\perp(\cdot) = \mathcal{I}(\cdot) - \Pi(\cdot)$, where $\Pi(\cdot)$ is the L^2 projection onto the finite element space and $\mathcal{I}(\cdot)$ the identity operator. See [8] for the computation of the stabilization parameters τ_1 and τ_2.

The time discretization is obtained using the backward Euler scheme for both the fluid and the structure equations. By defining the backward Euler operator δ_t as $\delta_t f^{n+1} = (f^{n+1} - f^n)/\delta t$ and denoting by $\mathrm{Ext}_h(\cdot)$ a discretized version of the extension operator $\mathrm{Ext}(\cdot)$, at each time level t^{n+1}, the **fully discretized fluid-multi structure interaction problem** reads:

(i) Geometry: find the fluid domain displacement so that

$$\mathcal{A}_{t^{n+1}}(\boldsymbol{x}_0) = \boldsymbol{x}_0 + \mathrm{Ext}_h(\hat{\boldsymbol{\eta}}_{i,h}^{n+1}|_{\Sigma_0^{fi}}),\ i=1,2,$$
$$\boldsymbol{w}_h^{n+1} = \delta_t \mathcal{A}_{t^{n+1}} \circ \mathcal{A}_{t^{n+1}}^{-1},\ \Omega_{t^{n+1}}^f = \mathcal{A}_{t^{n+1}}(\Omega_0^f). \tag{9}$$

(ii) Fluid-structure interaction: find $(\boldsymbol{u}_h^{n+1}, p_h^{n+1}, \hat{\boldsymbol{\eta}}_{1,h}^{n+1}, \hat{\boldsymbol{\eta}}_{2,h}^{n+1}) \in V_h^f \times Q_h \times \hat{V}_h^1 \times \times \hat{V}_h^1$ such that

$$\rho_f \left(\delta_t \boldsymbol{u}_h^{n+1}\big|_{\boldsymbol{x}_0}, \boldsymbol{v}_h^f \right)_{\Omega_{t^{n+1}}^f} + \mathcal{N}_s \left(\boldsymbol{u}_h^{n+1} - \boldsymbol{w}_h^{n+1}; \boldsymbol{u}_h^{n+1}, p_h^{n+1}, \boldsymbol{v}_h^f, q_h \right)_{\Omega_{t^{n+1}}^f}$$
$$= \left\langle \boldsymbol{f}_f^{n+1}, \boldsymbol{v}_h^f \right\rangle_{\Omega_{t^{n+1}}^f} \tag{10a}$$

$$\rho_1 \left(\frac{\hat{\boldsymbol{\eta}}_{1,h}^{n+1} - 2\hat{\boldsymbol{\eta}}_{1,h}^{n} + \hat{\boldsymbol{\eta}}_{1,h}^{n-1}}{\delta t^2}, \hat{\boldsymbol{v}}_h^1 \right)_{\Omega_0^1} + \left\langle \hat{\boldsymbol{\sigma}}_1^{n+1}, \nabla \hat{\boldsymbol{v}}_h^1 \right\rangle_{\Omega_0^1} = \left\langle \hat{\boldsymbol{f}}_1^{n+1}, \hat{\boldsymbol{v}}_h^1 \right\rangle_{\Omega_0^1}$$
$$- \left\langle \mathcal{R}_f(\boldsymbol{u}_h^{n+1}, p_h^{n+1}), \mathcal{E}_h^{f1}(\boldsymbol{v}_h^1|_{\Sigma_t^{f1}}) \right\rangle_{\Omega_{t^{n+1}}^f} - \langle \mathcal{R}_2(\hat{\boldsymbol{\eta}}_{2,h}^{n+1}), \mathcal{E}_h^{12}(\hat{\boldsymbol{v}}_h^1|_{\Sigma_0^{12}}) \rangle_{\Omega_0^2} \tag{10b}$$

$$\rho_2 \left(\frac{\hat{\boldsymbol{\eta}}_{2,h}^{n+1} - 2\hat{\boldsymbol{\eta}}_{2,h}^{n} + \hat{\boldsymbol{\eta}}_{2,h}^{n-1}}{\delta t^2}, \hat{\boldsymbol{v}}_h^2 \right)_{\Omega_0^2} + \left\langle \hat{\boldsymbol{\sigma}}_2^{n+1}, \nabla \hat{\boldsymbol{v}}_h^2 \right\rangle_{\Omega_0^2} = \left\langle \hat{\boldsymbol{f}}_2^{n+1}, \hat{\boldsymbol{v}}_h^2 \right\rangle_{\Omega_0^2}$$
$$- \left\langle \mathcal{R}_f(\boldsymbol{u}_h^{n+1}, p_h^{n+1}), \mathcal{E}_h^{f2}(\boldsymbol{v}_h^2|_{\Sigma_t^{f2}}) \right\rangle_{\Omega_{t^{n+1}}^f} \tag{10c}$$

$$\boldsymbol{u}_h^{n+1} = \delta_t \hat{\boldsymbol{\eta}}_{i,h}^{n+1} \circ \mathcal{A}_{t^{n+1}}^{-1} \quad \text{on } \Sigma_t^{fi},\ i=1,2, \tag{10d}$$

$$\delta_t \hat{\boldsymbol{\eta}}_{1,h}^{n+1} = \delta_t \hat{\boldsymbol{\eta}}_{2,h}^{n+1} \quad \text{on } \Sigma_0^{12}, \tag{10e}$$

for all $(\boldsymbol{v}_h^f, q_h, \hat{\boldsymbol{v}}_h^1, \hat{\boldsymbol{v}}_h^2) \in V_{0,h}^f \times Q_h \times \hat{V}_h^1 \times \hat{V}_{0,h}^2$.

See [2] for more details.

2.4. **Solution of the monolithic system.** To deal with the nonlinearities in the problem which are due to domain motion and to the convective term in (10a), a fixed point algorithm is employed. The linearization of the fluid-structure interaction problem (9)-(10) by the fixed point algorithm uses $\widetilde{\boldsymbol{\eta}}_{1,h}^{n+1}$ and $\widetilde{\boldsymbol{\eta}}_{2,h}^{n+1}$ (predictions for $\boldsymbol{\eta}_{1,h}^{n+1}$ and $\boldsymbol{\eta}_{2,h}^{n+1}$) to compute $\Omega_{t^{n+1}}^f$ and $\widetilde{\boldsymbol{u}}_h^{n+1}$ (predictions for $\boldsymbol{u}_h^{n+1}$) as convective velocity. More details can be found in [3]. The monolithic linearized system which results at every fixed point iteration is then solved by an extension of the ILUT-GMRES method proposed in [2].

We rely on a single finite element partition of the overall domain, which implies matching grids on the fluid-structure and structure-structure interfaces. The structure equations are reformulated in terms of velocity instead of displacement in order to define the fluid-structure interaction problem on the entire domain in terms of velocity. The same finite element spaces are then used for fluid velocity and structure velocity. Moreover, since a stabilization technique is used to circumvent the discrete inf-sup condition, the same finite element interpolation space can be used for the pressure unknowns as well. In particular, for the numerical simulation of the problem discussed in Section 3, we used $\mathbb{P}_1 - \mathbb{P}_1$ finite elements [19] for the fluid and $\mathbb{P}_1$ finite elements for the structures.

In this framework, the fluid-structure and structure-structure coupling conditions (the transmission conditions) are easily implemented. The kinematic coupling condition describing continuity of velocities on each interface is implicitly enforced

by the finite element space interpolation used over the whole domain. In particular, we adopt continuous finite element spaces, so the continuity of velocities at the interface is enforced automatically by the fact that there is only one value of the velocity at the interface nodes. The dynamic coupling condition describing continuity of stresses is imposed weakly. The weak transmission of stresses simply arises from the fact that shape functions on the interface nodes have support on the fluid and structure subdomains (fluid-structure interface) or on both structure subdomains (structure-structure interface). This way the final system has the simple form similar to the one described in [3, 2].

Standard preconditioned iterative methods were then used to solve the resulting monolithic system. In particular, we used the GMRES algorithm [21] preconditioned in two steps: first a diagonal scaling is applied and then the resulting system is preconditioned by an incomplete LU factorization (ILUT preconditioner). See [2] for details.

The numerical method presented in this section will be used in the next section to analyze the flow conditions associated with the ascending aortic anastomosis of LVAD cannula.

3. **Numerical characterization of flow conditions in LVAD cannula anastomosis.** Left Ventricle Assist Devices (LVADs) are implantable mechanical pumps that temporarily aid the function of the left ventricle. An LVAD is typically connected to the left ventricle apex and then anastomosed to the ascending aorta, as shown in Figure 2. Implantation of LVADs has been associated with throm-

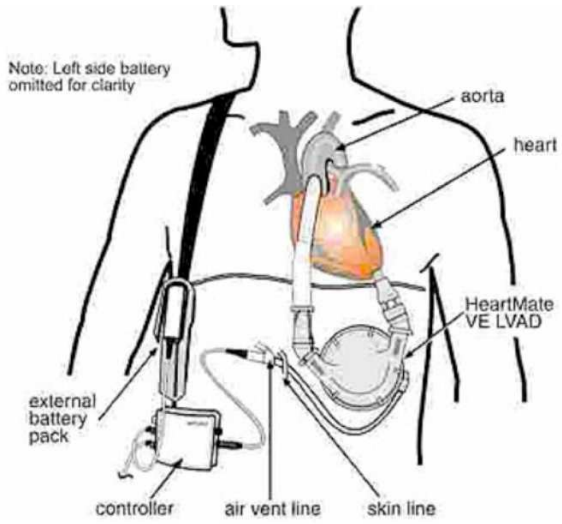

FIGURE 2. Left Ventricular Assist Device with anastomosis to ascending aorta.

bus formation close to the anastomosis region in the ascending aorta and next to the aortic valve, especially if native cardiac function is negligible and the aortic valve remains closed throughout cardiac cycle [10]. Stagnation points and recirculation zones have been implicated as the main fluid dynamics factors contributing to thrombus formation. In the present work we employ the fluid-structure interaction

algorithm described in Section 2.4 to simulate the fluid dynamics conditions in the anastomosis cannula and in the ascending aorta between the aortic valve and the anastomosis region. Clinicians have been trying to understand the optimal location of the cannula suture with respect to the aortic valve location that would minimize complications associated with thrombus formation, especially near the aortic valve leaflets.

In this work we investigate the stagnation and recirculation zones quantified by the stagnation index and vorticity index defined below. Of particular interest are the flow conditions generated by the cannula placement at 4, 5 and 6 cm from the aortic valve (clinical placement is typically 5 cm from the aortic valve), and with the cannula sutured to the ascending aorta at the angles of 30° and 90° (clinical suture is typically performed at 90°). Additionally, we have investigated how inclusion of the compliance of ascending aorta and a different compliant behavior of the anastomosis cannula influence the fluid flow simulations, stagnation zones and vorticity.

3.1. **Problem set up.** A realistic three-dimensional simulation of the fluid dynamics at the LVAD ascending aortic anastomosis with compliant aorta, LVAD cannula, and functional aortic leaflets, is exceedingly complicated. Often times various simplifying assumptions are made in order to obtain an insight into the corresponding fluid dynamics in a reasonable time frame. Although these simplifying assumptions bring a certain degree of idealization to the problem, the flow analysis of the simplified problem still provides important information about the main qualitative features of the underlying problem.

In this work we performed two-dimensional fluid flow simulations for the geometry corresponding to a section of the anastomosis cannula and the region of the ascending aorta from the closed aortic valve to an area downstream from the anastomosis, as shown in Figure 3(d). Three different combinations of structures compliant properties were considered:

(a) rigid aortic wall and cannula;
(b) compliant aortic wall and rigid cannula;
(c) compliant aortic wall and cannula.

The corresponding domains are shown in Figure 3(a)-(c).

The $2d$ domain assumes an idealization of the aortic geometry and of the aortic valve, ignoring the tricuspid geometry of the aortic valve leaflets. The $2d$ Navier-Stokes equations for an incompressible, viscous Newtonian fluid were coupled with the following equation of linear elasticity to describe the motion of the compliant boundaries

$$\rho_i D_t^2 \hat{\boldsymbol{\eta}} - \nabla \cdot (\mu_\ell^i (\nabla \hat{\boldsymbol{\eta}} + (\nabla \hat{\boldsymbol{\eta}})^T) + \lambda_\ell^i (\nabla \cdot \hat{\boldsymbol{\eta}}) I) + a_i \hat{\boldsymbol{\eta}} = \hat{\boldsymbol{f}}_i. \tag{11}$$

This structure model can be obtained from the equations of 3D linear elasticity assuming cylindrical geometry. The term which accounts for the effects of cylindrical geometry is the reaction term $a_i \hat{\boldsymbol{\eta}}$ in (11), where $a_i = E_i/(1-\nu_i^2)R^2$, E_i being the Young modulus, ν_i the Poisson ratio of the i-th structure, and R the distance of the structure from the axis of symmetry. This term plays an important role in recovering the physiologically reasonable pressures when elastic structures are considered since it accounts for the circumferential stress coming from the $3d$ geometry and should therefore not be neglected in the $2d$ simulations.

In this work the case of severe cardiac failure is considered, where native cardiac function may be negligible, and the aortic valve remains closed as all systemic

perfusion is provided by the LVAD. In these conditions thrombus formation is most likely. This is one reason why compliance of the aortic leaflets was not taken into account. Another reason why compliance of the aortic leaflets was not taken into account has to do with dimension reduction from $3d$ to $2d$. As mentioned above, the reaction term in the structure model (11) contains a coefficient which becomes singular as $R \to 0$ at the valve commissure where the leaflets meet. Even though there are ways to get around this difficulty in $2d$, this was not done in the present paper as we are currently extending our investigation to involve $3d$ simulations, in which case the singularity in the structure model at the valve commissures is no longer present. Other factors, however, related to $3d$ FSI simulations of the aortic valve motion make this problem exceedingly complicated and will not be addressed in the present manuscript.

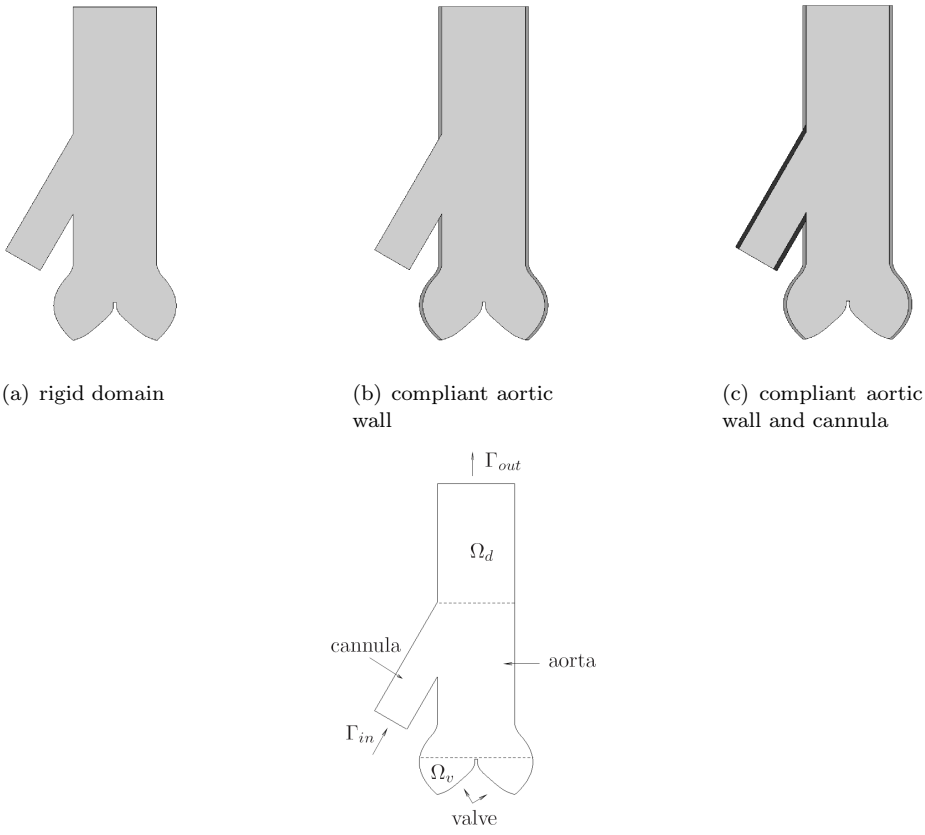

(a) rigid domain

(b) compliant aortic wall

(c) compliant aortic wall and cannula

(d) geometry

FIGURE 3. Computational domain for the simulations with (a) rigid boundaries, (b) deformable aortic wall and rigid cannula, (c) deformable aortic wall and cannula. (d) Explanation of the geometry.

The fluid and the structures physical parameters used in this manuscript are listed in Table 1. The LVAD cannula is made of polyvinyl chloride (dacron), whose

Young modulus in much higher than that of the aortic wall. Thus, we expect that accounting for the cannula compliance will not make much difference in the fluid dynamics. However, problem (c) is useful to test how the properties of the cannula material affect the flow conditions. The diameter of the LVAD cannula is taken to be 1.2 cm, while the diameter of the aorta is assumed to be 2.5 cm.

At the inlet of the anastomosis cannula the following Dirichlet condition for the velocity is imposed

$$\begin{aligned} \boldsymbol{u}\cdot\boldsymbol{n} &= -\left(40+\cos\left(\frac{\pi t}{0.5}-\frac{\pi}{2}\right)\right)\ \text{cm/s}, \\ \boldsymbol{u}\cdot\boldsymbol{t} &= 0, \end{aligned} \tag{12}$$

describing time-periodic inflow parallel to the walls of the cannula. Here $\boldsymbol{n}$ and $\boldsymbol{t}$ are the unit vectors normal and tangent to the inflow boundary, respectively (see Figure 3(d)). The magnitude of the velocity has been chosen to recover a flow rate of $5.45-5.56$ l/min, which is associated with a GYRO flow pump working at 2000 rpm [5]. Moreover, with this inlet boundary condition a Reynolds number (based on the diameter of the aorta) of 4200 was recovered, which is reasonable for blood flow in the ascending aorta. The algorithm presented in Section 2 with the appropriate choice of discretization performs well for such Reynolds numbers as was shown in [18] where a classical test problem of a wall-driven cavity flow [1] at Reynolds numbers up to 10^4 was studied.

Notice that condition (12) is periodic with period 1 s (we are assuming a pulsatile pump), which is approximately the duration of a cardiac cycle. On the outflow section we impose a non-homogeneous Neumann condition:

$$\boldsymbol{\sigma}\cdot\boldsymbol{n} = -p\boldsymbol{n}+\mu(\nabla\boldsymbol{u}+(\nabla\boldsymbol{u})^T)\cdot\boldsymbol{n} = 80\ \text{mmHg} = 106658\ \text{dyne/cm}^2,$$

this value being physiological. Notice that the use of this outlet condition does not imply constant pressure in the aorta, as the pressure is just one component of the normal stress. The pressure itself will be time-dependent as a consequence of boundary condition (12). In addition, since the valve is not displacing, a homogeneous Dirichlet condition is imposed on it. Whenever a compliant structure is present, its displacement is kept fixed at the inlet and at the outlet (proximal and distal ends), while a homogeneous Neumann condition is imposed on the rest of the physical boundary. The condition of fixed structure ends has been chosen for simplicity, even though it is unphysical and leads to small oscillations due to a boundary layer formed in a small neighborhood of the end points. More realistic structure boundary conditions will be studied in the future.

For the space discretization of the fluid we use stabilized $\mathbb{P}_1-\mathbb{P}_1$ finite elements. Whenever one or more structures are present, matching meshes were implemented at the interfaces and $\mathbb{P}_1$ finite elements were used for space discretization. The mesh of the fluid domain is the same for problems (a), (b), and (c), and consists of 6215 nodes and 11237 triangles. For the structure triangulations of problems (b) and (c) a diameter of 0.025 is taken. A time step $\delta t = 0.02$ s is set for all the simulations.

The enormous amount of information given by the numerical simulations needs to be synthesized in indexes, which aim at measuring some quantity of interest. For the problems under consideration we propose a *downstream zone vorticity index*

$$I_\omega = \sqrt{\frac{\int_{\Omega_d}|\nabla\times\boldsymbol{u}|^2\,d\Omega}{\int_{\Omega_d}d\Omega}}, \tag{13}$$

TABLE 1. Fluid and structure physical properties for the numerical tests

Fluid	
Density: $\rho_f = 1.0$ g/cm^3	Viscosity: $\mu = 0.035$ poise
Aortic wall	
Density: $\rho_s = 1.2$ g/cm^3	Thickness: $h_s = 0.1$ cm
Young modulus: $E = 6.5 \cdot 10^7$ dyne/cm^2	Poisson ratio: $\nu = 0.49$
LVAD cannula	
Density: $\rho_s = 1.37$ g/cm^3	Thickness: $h_s = 0.1$ cm
Young modulus: $E = 2.2 \cdot 10^{10}$ dyne/cm^2	Poisson ratio: $\nu = 0.43$

to measure the mean vorticity downstream from the anastomosis in the region indicated by Ω_d in Figure 3(d), and a *valve zone stagnation index*

$$I_s = \sqrt{\frac{\int_{\Omega_v} |\boldsymbol{u}|^2 \, d\Omega}{\int_{\Omega_v} d\Omega}}, \tag{14}$$

to quantify the region of stagnant flow close to the valve (denoted by Ω_v in Figure 3(d)). Index I_s represents the mean velocity over Ω_v.

Index (13) needs to be minimized in order to have a smooth laminar flow in the ascending aorta. On the other hand, index (14) has to be as high as possible to avoid flow stagnation, which is associated with clot formation.

3.2. **Significance of wall compliance.** In the first set of simulations we have investigated the importance of wall compliance on downstream vorticity and on flow stagnation in the aortic valve region. We assume that the anastomosis cannula is inserted into the aorta at a distance of 5 cm from the proximal end, and at an angle of 30° (see Figure 3(d)). It was shown in [15] that such an angle reduces **local** flow recirculation and high shear stress on the aortic wall, typical of high angle of insertion.

We have generated the flow conditions corresponding to the 3 different structure configurations: (a), (b), and (c), stated in the previous section. Fig. 4 shows the downstream zone vorticity index I_ω and the valve zone stagnation index I_s as functions of time, for problems (a), (b), and (c). Fig. 4(a) shows that I_ω oscillates around a mean value, with different amplitudes and phases if the aortic wall and cannula are modeled as rigid or if their elasticity is taken into consideration. The mean value of I_ω is 75.3 for problem (a), 73.7 for problem (b) and 71.9 for problem (c). Moreover, I_ω for problem (a) displays oscillations of larger amplitude. This means that the compliance of the structures surrounding the fluid naturally tends to reduce the magnitude of the vorticity.

Similarly, the values of I_s, shown in Figure 4(b), change for the three problems, depending on whether or not the compliance of the walls has been taken into account. The results shown in Figure 4(b) show that the compliance of the aortic wall and cannula increase the mean fluid velocity near the aortic valve, i.e., over Ω_v, for the whole duration of a cardiac cycle.

This shows that compliance of the cardiovascular tissue acts as a natural inhibitor of pathological flow conditions conducive to thrombus formation and should not be neglected in the computer simulations.

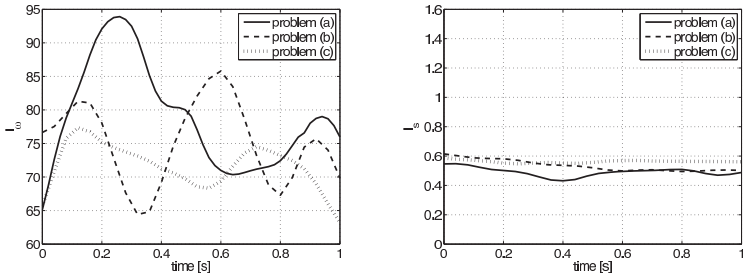

(a) downstream zone vorticity index (b) Valve zone stagnation index

FIGURE 4. (a) Downstream zone vorticity index I_ω and (b) valve zone stagnation index I_s for the problem with rigid boundaries (problem (a)), the problem with compliant aortic wall and rigid cannula (problem (b)), and the problem with compliant aortic wall and cannula (problem (c)).

In the rest of the paper all the simulations will account for the compliance of both the aortic wall and the cannula.

4. **Sensitivity of the valve stagnation index to the position of the anastomosis, material of the cannula and insertion angle.** Sensitivity of the stagnation index I_s to the variations in the position of the anastomosis, material of the cannula, and angle of insertion is considered. Three positions of the anastomosis: at a distance of 4, 5, and 6 cm from the aortic valve; two materials for the cannula: dacron and a material with the same properties as the aortic wall (see Table 1); and two angles of insertion: 30° and 90°, were tested.

Figure 5 shows the graphs of the stagnation index I_s for the three different positions and for the two different materials. The angle of insertion is kept at 30°. The graphs in Figure 5 show that the lower position of the cannula anastomosis guarantees a value of I_s above 1 cm/s for the entire cardiac cycle. This is due to the fact that the vortex generated by the blood stream coming from the cannula generates secondary vortices in the aortic sinuses (see Fig. 6 (a)). If the anastomosis is placed farther from the valve, the secondary vortices move progressively out of the sinuses (see Fig. 6 (b)). In the case of anastomosis located 6 cm away from the valve (upper anastomosis), shown in Fig. 6 (c), only the tertiary vortices enter the sinuses. The graphs in Figure 5 show that the insertion of the anastomosis cannula closest to the aortic valve provides the lowest likelihood for the formation of stagnant flow near the closed aortic valve, as expected.

Next, the sensitivity of I_s to the cannula material was studied. It was found that the cannula made of a material with the same properties (density, Youngs modulus and Poisson ratio) as the aortic wall, instead of a dacron cannula, does not significantly reduce the likelihood of stagnant flow formation near the aortic valve. Fig. 5 shows that the values of I_s associated with the softer cannula are comparable with those obtained for the dacron cannula for the upper and middle positions, while whey are smaller for the lower position. Therefore, the use of softer cannula instead of the dacron one does not improve the behavior of the stagnation index I_s near a closed aortic valve.

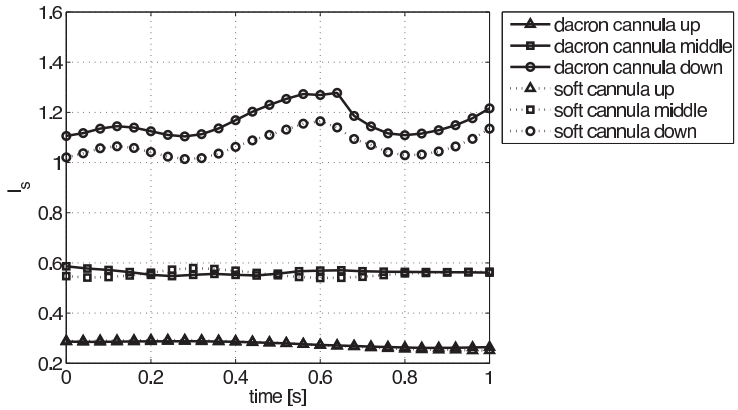

FIGURE 5. Comparison of the valve zone stagnation index I_s for three different positions of the anastomosis and two different materials for the cannula. The angle of insertion is 30° in all the cases.

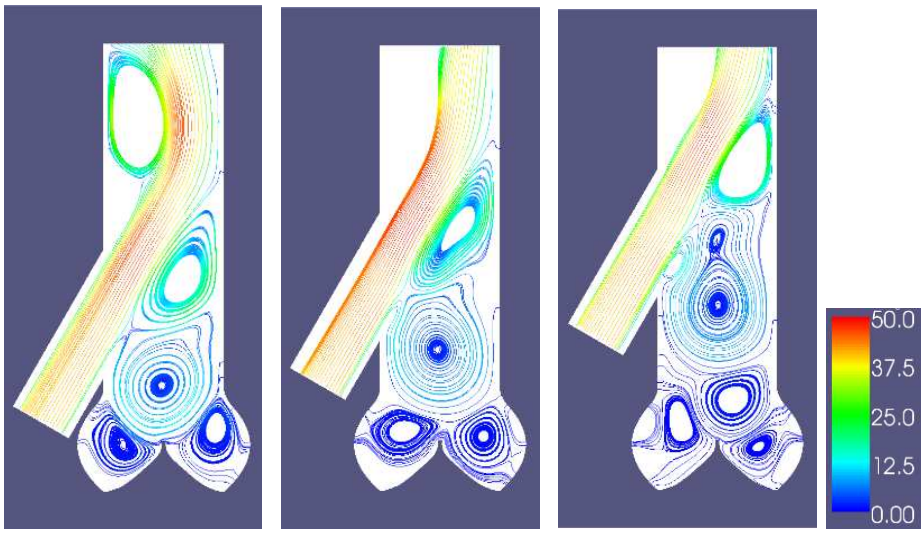

(a) lower anastomosis (b) middle anastomosis (c) upper anastomosis

FIGURE 6. Streamlines at the end of one cardiac cycle for (a) lower anastomosis, (b) middle anastomosis, and (c) upper anastomosis. The angle of insertion is 30° and the cannula is made of dacron. The streamlines are colored based on the velocity magnitude (in cm/s).

Finally, the sensitivity of I_s on the cannula insertion angle was studied. Fig. 7 shows I_s for different angles of insertions and different materials for the cannula for all three anastomosis positions (4, 5, and 6 cm from the aortic valve). Fig. 7 shows that the angle of insertion of 90° significantly lowers the values of I_s, regardless of

TABLE 2. Mean values of I_ω for three different positions of the anastomosis and two cannula material with angle of insertion of 30°.

	lower anastomosis	middle anastomosis	upper anastomosis
dacron cannula	74.1	71.9	66.4
soft cannula	73.8	71.8	66.2

the cannula material. It can be seen in Fig. 8(a) that this configuration distorts the primary vortex at the anastomosis which then, in turn, distorts the secondary vortices. The secondary vortex close to the anastomosis is "pulled out" of the aortic sinus, leaving a large region of stagnant flow behind. The distortion of the vortices is clear when Fig. 8(a) is compared with Fig. 6(a). Fig. 7(b) also shows that for the middle anastomosis the angle of insertion of 90° causes a reduction of I_s, both for dacron and soft cannula. Notice that the curves of I_s for the 90° cannula in the middle position are slightly higher than the corresponding ones in the lower position. This is because the vortices get less and less distorted as the cannula, placed at 90°, is moved up to the middle location in the ascending aorta (see Fig. 8). For the upper position of the anastomosis the values of I_s, reported in Figure 7(c), are slightly higher for the whole simulated cardiac cycle when the angle of insertion is 90°, independently of the cannula material.

Based on the results from Fig. 7 the optimal location for the anastomosis cannula that lowers the likelihood of stagnant flow near the aortic valve is the one closest to the aortic valve, inserted at the angle of 30° with respect to the native aorta. The graphs in Fig. 7 also indicate that the stagnation index I_s is not significantly influenced by the properties of the cannula material.

5. **Sensitivity of the downstream zone vorticity index to the position of the anastomosis, material of the cannula and insertion angle.** A sensitivity analysis to the variations in the position of the anastomosis, material of the cannula, and angle of insertion was performed for the vorticity index I_ω. We tested the same three positions of the anastomosis, two materials for the cannula, and two angles of insertion considered in Sec. 4 for the sensitivity index.

Figures 9(a) and (b) show the graphs of the vorticity index I_ω for the three different positions with dacron cannula and soft cannula, respectively. The angle of insertion is kept at 30°. The mean value of I_ω for every configuration considered in Fig. 9 is reported in Table 2. Fig. 9 and Table 2 suggest that by moving the anastomosis farther from the valve, the magnitude of the vorticity is reduced and a flow closer to laminar is obtained. However, notice that the vorticity index (Eq. (13)) is defined in the region downstream of the anastomosis all the way to the outlet flow boundary (see Fig. 3(d)). This means that in the case when the anastomosis is further away from the outlet boundary, the flow has more room to develop, showing secondary and tertiary vertices downstream from the anastomosis, and less influence of the outlet boundary on the flow conditions in the vicinity of the anastomosis. See Figure 10. A larger downstream flow region should be included for a thorough investigation of the vorticity influenced by the different positions of the cannula, which is beyond the scope of this manuscript.

Concerning the sensitivity of I_ω to the cannula material, it was found that the cannula made of a material with the same properties (density, Youngs modulus and

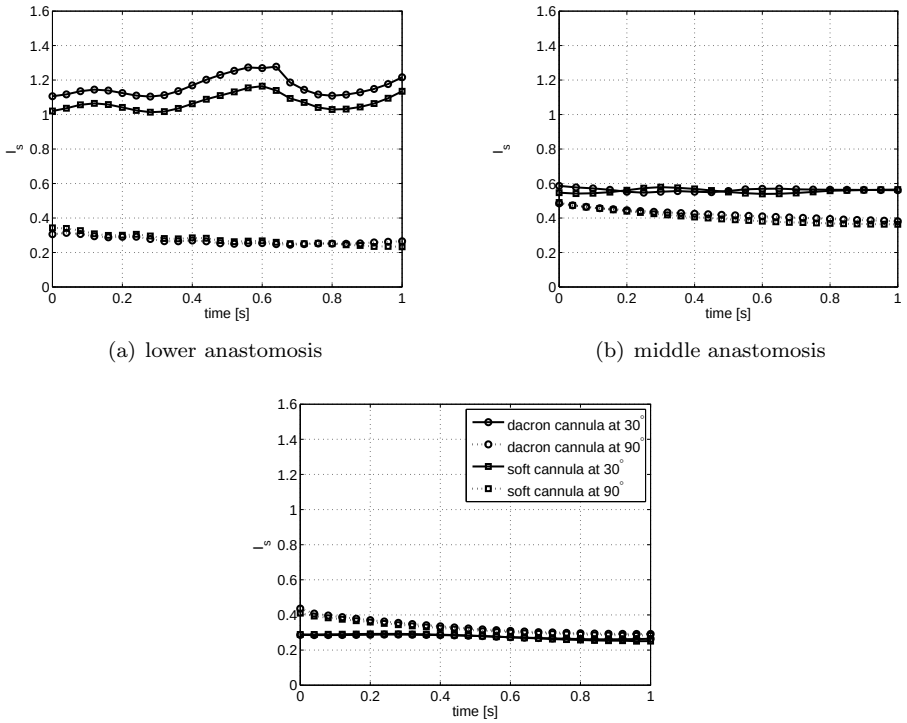

(a) lower anastomosis

(b) middle anastomosis

(c) upper anastomosis

FIGURE 7. Comparison of the valve zone stagnation index I_s for two different angles of insertion and two different materials for the cannula for (a) lower anastomosis, (b) middle anastomosis, and (c) upper anastomosis. The legend in (c) is common to the three subfigures.

Poisson ratio) as the aortic wall, instead of a dacron cannula, does not significantly reduce vorticity. Table 2 shows that the mean values of I_ω associated with the softer cannula are comparable with those obtained for the dacron cannula for all the positions of the anastomosis. Moreover, from Fig. 9 we see that I_ω displays oscillations of similar amplitude and only a small phase lag (oscillations are retarded by the softer material) when the position of the anastomosis is the same and the cannula material is different. The phase lag gets smaller as the anastomosis approaches the valve. We can conclude that the use of a softer cannula instead of the dacron one does not improve the quality of the flow in the aorta.

Finally, the sensitivity of I_ω on the cannula insertion angle was studied. Fig. 11 shows I_ω for different angles of insertions and different cannula materials for all three anastomosis positions (4, 5, and 6 cm from the aortic valve). Fig. 11 shows that the angle of insertion of 90° significantly increases the values of I_ω, regardless of the cannula material. The mean value of I_ω for each configuration with angle of insertion of 90° is reported in Table 3. Every value in Table 3 is between 35% and 55% higher than the correspondent value in Table 2, proving that increasing the angle of insertion from 30° to 90° worsen the quality of the flow in the aorta.

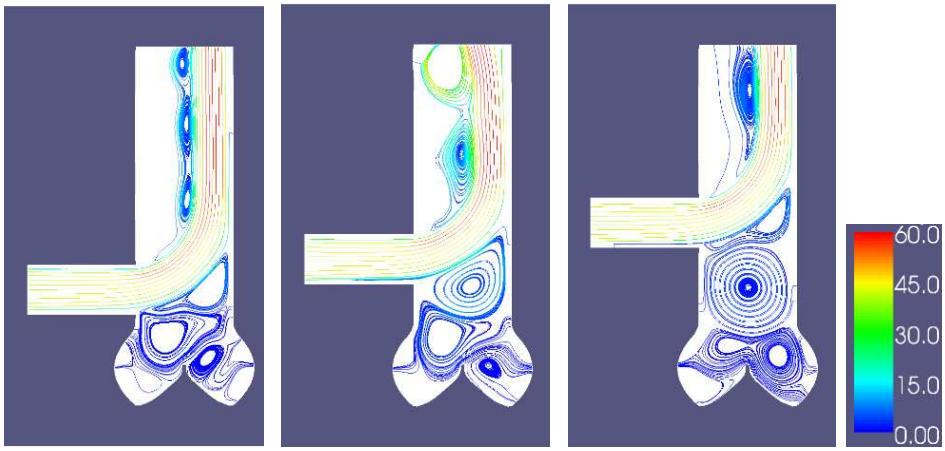

(a) lower anastomosis (b) middle anastomosis (c) upper anastomosis

FIGURE 8. Streamlines at the end of one cardiac cycle for (a) lower anastomosis, (b) middle anastomosis, and (c) upper anastomosis. The angle of insertion is 90° and the cannula is made of dacron. The streamlines are colored based on the velocity magnitude (in cm/s).

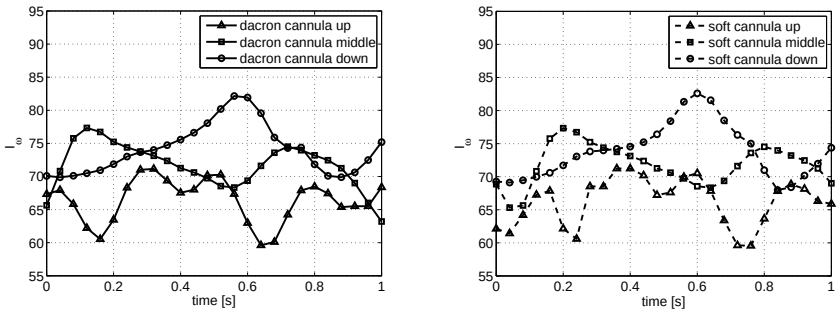

(a) dacron cannula (b) soft cannula

FIGURE 9. Comparison of the downstream zone vorticity index I_ω for three different positions of the anastomosis with (a) dacron cannula and (b) soft cannula. The angle of insertion is 30° in all the cases.

Notice from Table 3 that the mean value of I_ω is almost independent of the position of the anastomosis, suggesting that the vorticity distribution does not change much with the distance from the anastomosis. The vorticity filed at a given time level for the three configurations at 90° is shown in Fig. 12.

Based on the results from the sensitivity analysis of the vorticity index, the optimal configuration found in Sec. 4 which minimizes the risk of thrombus formation based on the stagnation index values (lower anastomosis, 30° angle of insertion) is found to also provide the lowest vorticity formation in the flow downstream from

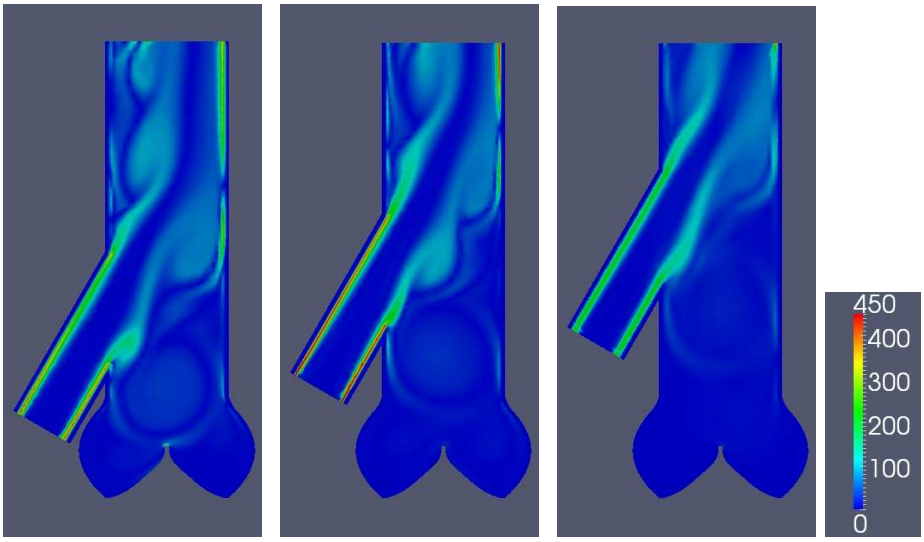

(a) lower anastomosis (b) middle anastomosis (c) upper anastomosis

FIGURE 10. Vorticity magnitude at the end of one cardiac cycle for (a) lower anastomosis, (b) middle anastomosis, and (c) upper anastomosis. The angle of insertion is 30° and the cannula is made of dacron.

TABLE 3. Mean values of I_ω for three different positions of the anastomosis and two cannula material with angle of insertion of 90°.

	lower anastomosis	middle anastomosis	upper anastomosis
dacron cannula	101.1	103.6	102.5
soft cannula	101.1	104.3	102.1

the anastomosis. In addition, our analysis shows that the vorticity index I_ω, like the stagnation index, is not significantly influenced by the properties of the cannula material.

6. **Conclusions.** We have implemented a novel fluid-structure interaction algorithm to study flow conditions associated with LVAD ascending aortic anastomosis. The proposed numerical algorithm is capable of capturing different elastic properties of the native aortic wall and of the LVAD cannula. The numerical method is based on a monolithic approach where fluid-structure and structure-structure interaction are treated in the same way: continuity of stresses is imposed in a weak sense while the continuity of velocity is imposed in the strong sense.

Flow conditions between the anastomosis location and the closed aortic valve exhibiting no function were studied. Two indexes were proposed to quantify the deviation from laminar flow downstream from anastomosis (the vorticity index) and to quantify the severity of stagnant flow near the aortic leaflets (the stagnation index). Deviation from laminar flow and formation of stagnation points has been implicated as the main fluid-dynamics factors responsible for thrombus formation.

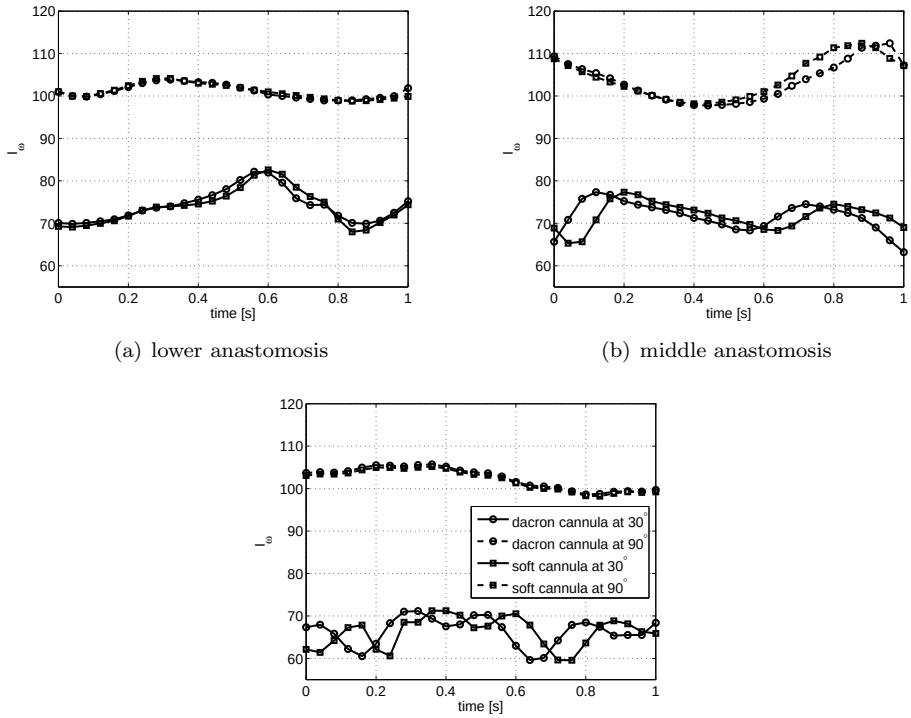

(a) lower anastomosis

(b) middle anastomosis

(c) upper anastomosis

FIGURE 11. Comparison of the dowstream zone vorticity index I_ω for two different angles of insertion and two different materials for the cannula for (a) lower anastomosis, (b) middle anastomosis, and (c) upper anastomosis. The legend in (c) is common to the three subfigures.

The study presented in this manuscript found that the cannula placement closest to the aortic valve (within 4 cm away from the valve) and at the angle of 30° with respect to the native aorta close to the aortic valve, gives rise to the flow conditions which are least likely to lead to thrombus formation. Rigidity of the dacron cannula was found to play almost no role in generating pathological conditions downstream from the anastomosis. Compliance of the native aortic wall was found to be important in naturally reducing the magnitude of vorticity, thereby lowering the probability of thrombus formation.

In contrast with other works in this area which include a study of flow conditions near anastomosis, ignore the aortic valve location, and almost excusively ignore the compliance of the aortic wall, the present study shows that all these factors are important in the analysis of optimal LVAD cannula placement.

Acknowledgments. The authors would like to thank the reviewers for their suggestions and comments that improved the quality of the manuscript.

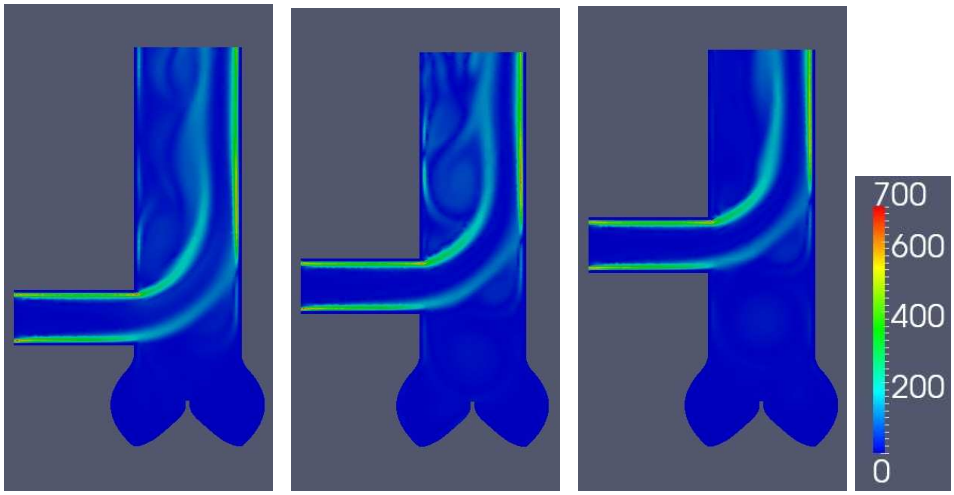

(a) lower anastomosis (b) middle anastomosis (c) upper anastomosis

FIGURE 12. Vorticity magnitude at the end of one cardiac cycle for (a) lower anastomosis, (b) middle anastomosis, and (c) upper anastomosis. The angle of insertion is 90° and the cannula is made of dacron.

REFERENCES

[1] F. Autieri, N. Parolini and L. Quartapelle, *Numerical investigation on the stability of singular driven cavity flow,* J. Comput Phys, **183** (2002), 1–25.

[2] S. Badia, A. Quaini and A. Quarteroni, *Modular vs. non-modular preconditioners for fluid-structure systems with large added-mass effect,* Comput. Methods Appl. Mech. Engrg., **197** (2008), 4216–4232.

[3] S. Badia, A. Quaini and A. Quarteroni, *Splitting methods based on algebraic factorization for fluid-structure interaction,* SIAM J. Sci. Comput., **30** (2008), 1778–1805.

[4] S. Badia, A. Quaini and A. Quarteroni, *Coupling Biot and Navier-Stokes equations for modelling fluid-poroelstic media interaction,* J. Comput. Phys., **228** (2009), 7986–8014.

[5] M. Behr, D. Arora, Y. Nosé and T. Motomura, *Performance analysis of ventricular assist devices using finite element flow simulation,* Int. J. Numer. Meth. Fluids, **46** (2004), 1201–1210.

[6] F. Brezzi and M. Fortin, "Mixed and Hybrid Finite Element Methods," Springer Series in Computational Mathematics, **15**, Springer-Verlag, New York, 1991.

[7] J. Coats, "A Manual Of Pathology," Longmans, Green, and Co., 1999.

[8] R. Codina, *Stabilized finite element approximation of transient incompressible flows using orthogonal subscales,* Comput. Methods Appl. Mech. Engrg., **191** (2002), 4295–4321.

[9] A. Cordero, S. Castaño and G. Rábago, *Prosthetic aortic valve thrombosis after Left Ventricular Assist Device implantation,* Rev. Esp. Cardiol., **58** (2005), 863.

[10] J. A. Crestanelloa, D. A. Orsinellib, M. S. Firstenberga and C. Sai-Sudhakar, *Aortic valve thrombosis after implantation of temporary Left Ventricular Assist Device,* Interactive Cardiovascular and Thoracic Surgery, **8** (2009), 661–662.

[11] L. Formaggia and F. Nobile, *A stability analysis for the arbitrary Lagrangian Eulerian formulation with finite elements,* East-West J. Num. Math., **7** (1999), 105–131.

[12] K. Fraser, T. Zhang, M. Ertan Taskin, B. P. Griffith, Z. J. Wu, F. Alamanni, E. G. Caiani and A. Redaelli, *Computational fluid dynamics analysis of thrombosis potential in Left Ventricular Assist Device drainage cannulae,* ASAIO J., in press, 2010.

[13] M. A. Gimbrone, *Endothelial disfunction, hemodynamic forces, and atherosclerosis (pubmed abstract),* Thrombos Haemost, **82** (1999), 722–726.

[14] B. Ker, R. M. Delgado III, O. H. Frazier, I. D. Gregoric, M. T. Harting, Y. Wadia, T. J. Myers, R. D. Moser and J. Freund, *The effect of LVAD aortic outflow-graft placement on hemodynamics and flow: Implantation technique and computer flow modeling,* Texas Heart Institute Journal, **32** (2005), 294–298.

[15] K. D. May-Newman, B. K. Hillen, C. S. Sironda and W. Dembitsky, *Effect of LVAD outflow conduit insertion angle on flow through the native aorta,* J. of Medical Engineering and Technology, **28** (2004), 105–109.

[16] A. L. Meyer, C. K. Kuehn, J. W. Weidemann, D. Malehsa, C. Bara, S. Fischer, A. Haverich and M. Strüber, *Thrombus formation in a HeartMate II Left Ventricular Assist Device,* Thoracic and Cardiovascular Surgery, **135** (2000), 203–204.

[17] F. Nobile, "Numerical Approximation of Fluid-Structure Interaction Problems with Application to Haemodynamics," Ph.D thesis, École Polytechnique Fédérale de Lausanne, 2001.

[18] A. Quaini, S. Canic, R. Glowinski, S. Little and W. Zoghbi, *The influence of the Coanda effect on the assessment of mitral valve regurgitation: A numerical investigation,* in preparation, 2010.

[19] A. Quarteroni and A. Valli, "Numerical Approximation of Partial Differential Equations," Springer Series in Computational Mathematics, **23**, Springer-Verlag, Berlin, 1994.

[20] A. G. Rose, J. H. Connelly, S. J. Park, O. H. Frazier, L. W. Miller and S. Ormaza, *Total left ventricular outflow tract obstruction due to Left Ventricular Assist Device induced sub-aortic thrombosis in 2 patients with aortic valve bioprosthesis,* Journal of Heart and Lung Transplantation, **22** (2003), 594–599.

[21] Y. Saad, "Iterative Methods for Sparse Linear Systems," 2nd edition, Society for Industrial and Applied Mathematics, Philadelphia, PA, 2003.

[22] D. Seiffge, *Thrombotic reactions of vascular anastomoses: Comparison of model studies with experimental findings,* Vasa Suppl., **32** (1991), 54–56.

[23] N. G. Smedira, *Invited commentary: Valve disease and LVAD,* Annals of Thoracic Surgery, **71** (2001), 1453.

Received June 9, 2010; Accepted September 13, 2010.

E-mail address: quaini@math.uh.edu
E-mail address: canic@math.uh.edu
E-mail address: davidpaniag@pol.net